Computers and Electronics in Agriculture 188 (2021) 106319

Contents lists available at ScienceDirect

Computers and Electronics in Agriculture

journal homepage: www.elsevier.com/locate/compag

Original papers

Intelligent thermal image-based sensor for affordable measurement of crop canopy temperature

Jaime Giménez-Gallego [a], Juan D. González-Teruel [a], Fulgencio Soto-Valles, PhD [a], Manuel Jiménez-Buendía, PhD [a], Honorio Navarro-Hellín, PhD [b], Roque Torres-Sánchez, PhD [a,*]

[a] Departamento de Automática, Ingeniería Eléctrica y Tecnología Electrónica (DAIETE), Technical University of Cartagena, Campus Muralla del Mar s/n, E-30202 Cartagena, Spain

[b] Widhoc Smart Solutions, Carretera del Albujon – Cabo de Palos, Km. 8 30593 La Palma, Cartagena, Spain

ARTICLE INFO

Keywords:
Precision agriculture
Deficit irrigation
CWSI
Thermography
Image segmentation

ABSTRACT

Crop canopy temperature measurement is necessary for monitoring water stress indicators such as the Crop Water Stress Index (CWSI). Water stress indicators are very useful for irrigation strategies management in the precision agriculture context. For this purpose, one of the techniques used is thermography, which allows remote temperature measurement. However, the applicability of these techniques depends on being affordable, allowing continuous monitoring over multiple field measurement. In this article, the development of a sensor capable of automatically measuring the crop canopy temperature by means of a low-cost thermal camera and the implementation of artificial intelligence-based image segmentation models is presented. In addition, we provide results on almond trees comparing our system with a commercial thermal camera, in which an R-squared of 0.75 is obtained.

1. Introduction

The optimization of irrigation water, which is the activity with the largest consumption of freshwater worldwide (Berni, 2009), is one of the major concerns in agriculture, being a limiting factor for crop yielding (Fernández García et al., 2020) in arid and semi-arid regions. In order to contribute to the optimization of crop water management, new irrigation strategies, such as Regulated Deficit Irrigation (RDI), have been developed to reduce the water consumption during non-critical periods (Azorín and García, 2020; Fereres and Soriano, 2006; Kannan and Anandhi, 2020; Noguera et al., 2020; Torres-Sanchez et al., 2020). Deficit irrigation techniques require the supervision of the plant water status through physiological indicators to avoid undesirable effects on crop yields (Azorín and García, 2020; Fereres and Soriano, 2006; Fernández García et al., 2020; Naor, 2000). The selection of these indicators is crucial since a balance must be found between the sensibility of measuring the crop water status and the capability to implement its measurement. Midday Stem Water Potential (SWP) is considered to be the parameter par excellence for the estimation of the crop water status (Naor, 2000). However, it is a destructive, non-automatable and very time-consuming method, which implies discontinuous measurements and the unfeasibility of scaling up to large plantations. Alternatively, other remotely and continuously measurable variables in soil, plant and atmosphere show sensitivity to crop water stress, allowing an indirect estimation of crop water status (Blonquist et al., 2009; González-Teruel et al., 2019; Torres-Sanchez et al., 2020). Plant-based continuous indicators, such as maximum daily branch shrinkage using dendrometers, are also used to estimate the crop water status and have been proven to be useful in irrigation management. Plant temperature is one of the most extended variables used in providing insight into crop water status. The stomatal aperture, which is influenced by plant and soil water status as well as meteorological conditions, affects the temperature of the leaves as it acts as a cooling mechanism by controlling the evapotranspiration (Blonquist et al., 2009). The higher the crop water stress, the lower the stomatal aperture in order to prevent the plant from water exhaustion, thus leading to an increase of leaf temperature. The Crop Water Stress Index (CWSI) (Idso et al., 1981; Jackson et al., 1981) is extensively used to account for the crop stress (Camino et al., 2018; García-Tejero et al., 2018; Krishna et al., 2019; Kullberg et al., 2017; Noguera et al., 2020; Poblete et al., 2018) by comparing the differences of temperature

* Corresponding author.
E-mail addresses: jaime.gimenez@upct.es (J. Giménez-Gallego), juando.gonzalez@upct.es (J.D. González-Teruel), pencho.soto@upct.es (F. Soto-Valles), manuel.jimenez@upct.es (M. Jiménez-Buendía), hono.navarro@gmail.com (H. Navarro-Hellín), roque.torres@upct.es (R. Torres-Sánchez).

https://doi.org/10.1016/j.compag.2021.106319
Received 13 May 2021; Received in revised form 26 June 2021; Accepted 3 July 2021
Available online 15 July 2021

between the air and canopy, fully transpiring leaf and non-transpiring leaf. Different procedures are used for the determination of fully transpiring and non-transpiring temperatures, such as those based on theoretical, virtual, meteorological, plant an artificial wet references (King and Shellie, 2016; Krishna et al., 2019; Maes et al., 2016). Nevertheless, wind speed and solar radiation are factors that influence the difference between leaf and air temperatures and that are not taken into account (Jones, 2018). There exist other stress indicators that are calculated from the canopy temperature, such as, Canopy Temperature Ratio (CTR) (Bausch et al., 2011), Degrees Above Non-Stressed (DANS) (Taghvaeian et al., 2014) and Degrees Above Canopy Threshold (DACT) (DeJonge et al., 2015). These indicators have been considered in recent years as an alternative to the CWSI, as they require few data to be calculated, which is an advantage for their practical application (Kullberg et al., 2017). Furthermore, the comparison of these methods was carried out in an experiment under deficit irrigation conditions by using different treatments and it was concluded that the obtained errors were similar to those with the CWSI (Kullberg et al., 2017).

It is crucial, in any case, to obtain the crop canopy temperature in order to estimate the crop water stress using the above-mentioned indicators. Several techniques can be found to measure the crop canopy temperature. Infrared radiometers are widely used and one of the most popular options providing remote measurement and field installation robustness. Nonetheless, the main drawback of infrared radiometers is that both emitted and reflected radiation from the different sources covered by the field of view is integrated in the bulk measurement, thus, impeding the determination of canopy temperature exclusively, and additional equipment is required in order to find a correct framing on the canopy (Blaya-Ros et al., 2019). Alternatively, thermography has been extensively used in this application in a variety of ways (Aasen et al., 2018; Berni et al., 2009; Camino et al., 2018; Costa et al., 2013; Fuentes et al., 2012; García-Tejero et al., 2018; Krishna et al., 2019; Kullberg et al., 2017) encompassing from handheld (Blaya-Ros et al., 2020; García-Tejero et al., 2018; Noguera et al., 2020), stationary on-site (Yang et al., 2009) or land vehicle-attached devices (Gutiérrez et al., 2018; Osroosh et al., 2018) to airborne vehicles (Berni et al., 2009; Blanco et al., 2020; Poblete et al., 2018) and satellites (Zhang et al., 2020). In the case of the latter, low spatial and temporal resolution is the major concern, whereas for drones, radiometric calibration, atmospheric corrections and geometric calibration of the optics and sensors for photogrammetry application is needed (Berni, 2009), in addition to limitations on flight autonomy. Moreover, expert technicians are required to perform the tests in both cases, making them more expensive and restrictive.

Image-based temperature measurement has to consider only the regions of the thermal image corresponding to the crop canopy when obtaining the water stress index (Camino et al., 2018; Fuentes et al., 2012; Poblete et al., 2018). This issue requires an image segmentation to carry out the Region Of Interest (ROI) extraction. Thermal image processing is limited due to the low resolution offered by thermal cameras, especially low-cost ones like the one used in this article. In addition, a marked thermal gradient between the elements to be segmented must exist. This poses a problem in the deficit irrigation scenario, where severely water-stressed crop canopy may be confused with elements that do not pertain to the ROI (Zhou et al., 2021). As a consequence, the segmentation process is usually performed on the visible image (Cerutti et al., 2015) and for that purpose, several image processing methods have been described in the literature, such as, Thresholding (Otsu, 1979), MeanShift (Cheng, 1995; Comaniciu et al., 2002), Pyramidal MeanShift (Li et al., 2010), Graphcut (Boykov and Jolly, 2001), Watershed (Dougherty et al., 2019), Snakes (Chan and Vese, 2001), B-splines Snake (Brigger et al., 2000), Grabcut (Rother et al., 2004), Felzenszwalb (Felzenszwalb and Huttenlocher, 2004), SLIC (Achanta et al., 2012), Kurtz's algorithm (Achanta et al., 2012), Weber's algorithm (Weber et al., 2011), Power Watershed (Couprie et al., 2009), GAC (Cerutti et al., 2013), RGB-D based segmentation (Xia et al., 2015) and, more recently, machine learning and deep learning (Giménez-Gallego et al., 2019; Singh and Misra, 2017; Ward et al., 2019; Zhou et al., 2021). Subsequently, a visible image camera and image matching strategies between the visible and thermal image are used to apply the generated mask to the temperature matrix. Furthermore, because the sensor can process the visible image, there is great potential for the future implementation of new agricultural application procedures. In this sense, a model can be applied for the segmentation between sunlit and shaded leaves, which is of interest in determining the water status of plants (Poblete et al., 2018). It would also be possible to implement an image classification model to determine the specific phenotype (Azlah et al., 2019) for which the measurement is to be made, thus allowing to use dedicated models to enhance the performance on image segmentation. Morphological shape and colourimetrical variations of the fruit (Li et al., 2016; Lin et al., 2019b, 2019a; Osroosh and Peters, 2019) are also possible indicators derived from visible image processing that can be used for optimal harvesting predictions or phenological stage estimation of the crop (Vicente-Guijalba et al., 2014).

Currently, several low-cost devices for the determination of the crop water status based on the measurement of the canopy temperature have been developed (García-Tejero et al., 2018; Noguera et al., 2020). However, a manual segmentation for the extraction of the ROI is required (García-Tejero et al., 2018) or lack the capacity to discriminate it as the sensor is not image-based (Noguera et al., 2020), which makes them unsuitable for continuous and autonomous measurement. In this paper, a novel thermal and visible image-based sensory platform is proposed. Automatic image processing based on previously developed machine learning and deep learning segmentation models (Giménez-Gallego et al., 2019) is implemented. Thus, an accurate continuous monitoring of crop canopy temperature is pursued. The visible image is used for segmentation, then the thermal one is matched and the temperature of the ROI is determined. This has previously been handled by RGB threshold-based image processing (Osroosh et al., 2018), but it lacks flexibility in terms of lighting conditions, image background and type of crop. The performance of the device is compared with that of a commercial thermal camera whose results have been manually processed to determine the ROI. Calibration, adjustment procedures and thermal image capture methodology are also discussed, as well as the influence of environmental conditions on the correct operation of the device. This paper is structured in four sections. Section two deals with the development of the sensor and the definition of the experiment whose results are presented and discussed in the third section. Finally, conclusions are outlined.

2. Materials and methods

2.1. Sensor description and operation

2.1.1. Sensor hardware

A low-cost hardware platform has been chosen for image-collection and data-processing. The Raspberry Pi 4 model B from Raspberry Pi Foundation (Station Road, Cambridge, UK) was used. It was operated under Linux and programmed under GNU Python language ("Python official website"). Regarding the RGB camera, the Raspberry Pi Camera Rev. 1.3 (5MP, 1080p) was used, conured with a resolution of 640x480 pixels. The thermal camera used was the FLIR Radiometric Lepton 3.5 from FLIR® Systems (Wilsonville, OR, USA), integrated into the PureThermal 1 - FLIR Lepton Smart I/O Module V1.3 with the GetLab (Reno, NV, USA) Y16 firmware. The thermal camera has an automatic shutter, a resolution of 160x120 pixels and an effective frame rate of 8.7 Hz. The operating temperature range spans from −10 to 80 °C and the measurement range in high gain mode from −10 to 140 °C, which meets the needs for measurements in the crop canopy temperature. The radiometric accuracy is ±5 °C and the thermal sensitivity <0.05 °C. Additionally, a switch to control the power, a LED indicating the sensor status, a push-button to perform the measurement process and another

push-button to close the program and put the Raspberry in standby mode were added to the system for user-interfacing purposes.

2.1.2. Case

The above-described elements were integrated into a custom-designed case manufactured by using a CR-10S Fused Deposition Modeling (FDM) printer (Shenzhen Creality 3D Technology Co., Ltd., JinChengYuan, Tongsheng Community, Dalang, Longhua District, Shenzhen, China), as shown in Fig. 1.

The case consists of two parts: the base, which includes a holder for the cameras and enough space for the Raspberry Pi and shields; and a casing, which fits over the previous one to protect the system. The camera holder was designed so that both thermal and visible images had the same orientation and height and were situated at a minimum distance. This ensures that the centres of the images are also at the same height, so that the imaginary lines perpendicular to the planes of the images and passing through their centres are cut, not crossed, and at a distance of 1 m from the cameras, defined by the relative angle between them, as depicted in Fig. 2.

2.1.3. Cameras calibration

Once the cameras were mounted on the holder and secured with screws, a slight error in the correspondence of the images was observed. Therefore, the content of the images was not identical and it was necessary to determine the common area between both cameras for image-corresponding. So, for real-time image processing, the thermal image would have to be analysed, in order to match both images to identify shapes or patterns that correspond to those of the visible image. Nevertheless, the problem that there is no clear relationship between the isothermal and monochrome regions arises. Thus, in a real field situation, it would be difficult to determine common singular points in the image. Moreover, this would mean an increase in the computational cost and, therefore, in the response time and consumption of the sensor. Consequently, it was decided to perform a calibration under laboratory conditions to obtain the intersection region between the thermal and visible images. The calibration consisted of identifying a significant pixel, namely the centroid of a calibration object easily recognizable by both cameras. In this case, a cooled blue rectangular block was used as the calibration object. Obtaining an image with each camera, it was converted to binary format by means of either a colour or a temperature threshold. Then, the calibration object contour and the centroid was determined, as shown in Fig. 3.

To obtain the common area in each frame, it would simply be necessary to crop both images according to the differences between the horizontal and vertical coordinates of the centroids. The calibration would only have to be repeated in case the relative position between the cameras was changed. This position is undisturbed if the designed holder is used, which also ensures the precise correspondence for the

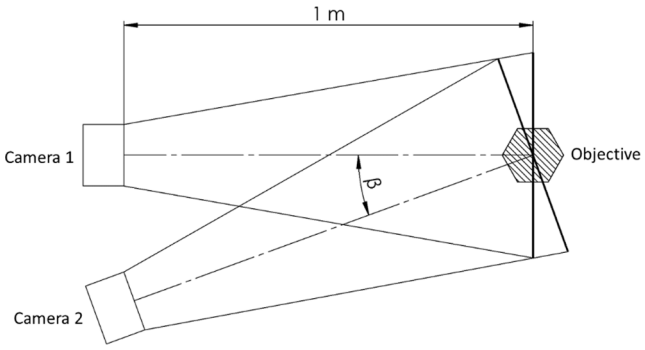

Fig. 2. Correspondence of the visible and thermal image centres through the holder.

lenses at a distance equal to that of the calibration object, chosen of 1 m in this study for convenience.

Regarding the cameras synchronization, a constant time difference was observed between the captures of both images, visible and thermal. This is critical, because the leaves may be moving in the wind, which would result in a mismatch. Hence, it was decided to delay the thermal camera to minimize the difference. To verify the synchronization between the sensor cameras, the time difference between the visible and thermal image captures was measured in 1000 frames. An average time difference of 11 ms was obtained. This time is considered to be sufficiently short to prevent external factors such as wind from interfering.

Furthermore, in order to correctly capture the visible image, an automatic camera brightness adjustment algorithm was designed, since situations of over-or under-lighting in the field may occur. Specifically, it was a Fuzzy controller, which, based on the mean intensity of the image's pixels, modified the camera's brightness.

2.1.4. Segmentation models implementation

Image segmentation on the visible image is required in order to discriminate the ROI. Once the correspondence with the thermal image was made, as defined above, the mask resulting from the segmentation was applied on the temperature matrix. Thus, the results were calculated considering only the values associated with pixels that had been classified as leaf by the segmentation model.

Two segmentation models were applied to generate the mask. The first one was a model based on the Support Vector Machine (SVM) supervised learning algorithm, generated from a dataset built with the help of a clustering plus manual classification process (Giménez-Gallego et al., 2019). The second model used was based on Deep Learning and the network architecture was SegNet (Giménez-Gallego et al., 2019). Originally, model inference was intended to be performed on the Raspberry Pi. To integrate these models developed in MATLAB (The

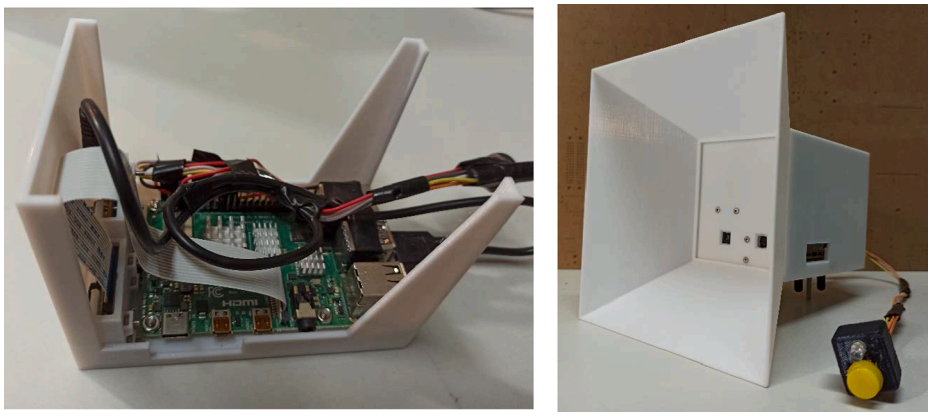

Fig. 1. Measuring system assembled in the case without cover (left) and with it (right).

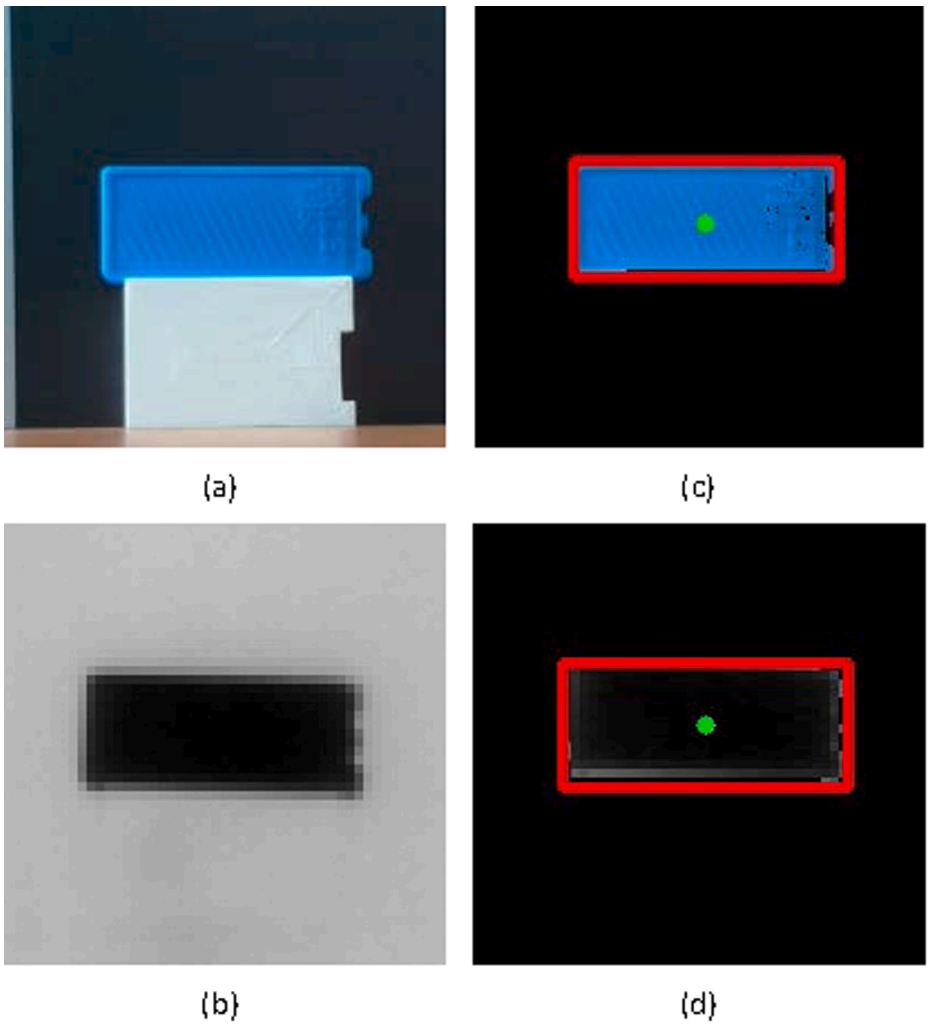

Fig. 3. Example of the calibration process for the correspondence of the visible and thermal images of the sensor: (a) visible image; (b) thermal image; (c) contour and centroid of segmented calibration object in visible image; and (d) contour and centroid of segmented calibration object in thermal image.

MathWorks, Inc., Natick, MA, USA) ("MATLAB official website"), it was necessary to generate them in Python. In the case of the Deep Learning model training, Keras 2.3.1 ("Keras Documentation") and Tensorflow 2.0 ("TensorFlow") were used, employing Mobilenet (Howard et al., 2017) as a backbone. Mobilenet is an efficient option for the implementation of artificial intelligence models in devices with limited processing capacity or in cases where time is a critical factor (Howard et al., 2017), since the computational cost to carry out the predictions is lower than that of other backbones such as ResNet (Bianco et al., 2018). The remote processing structure was chosen over the "in situ" option, as the heavy measurement analysis was a limit both in terms of computational capacity and power consumption of the sensor, if battery operated. The measurements were exported to a computer to perform the corresponding processing.

2.2. Experimental deployment

2.2.1. Reference thermal camera

To verify the performance of the proposed sensor, a comparative experiment with the commercial thermal camera FLIR SC305 (FLIR® Systems, Inc., Wilsonville, OR, USA), which has a resolution of 320x240 pixels, an accuracy of ± 2 °C and a thermal sensitivity <0.05 °C, was proposed. For the processing of the thermal images, the ThermaCam Researcher Professional v2.10 (FLIR® Systems, Inc., Wilsonville, OR, USA) software was used. The thermographic parameters of the camera were configured by setting an emissivity for the leaves of 0.98 (Chen, 2015; López et al., 2012; Maes et al., 2016), a distance from the subject of 1 m and measuring the ambient temperature and relative humidity by means of a weather station. Unfortunately, this camera does not offer the same field of view as the developed sensor. Therefore, in order to make a correct comparison of the results, images were cropped in order to overlap the results with the ones based on the FLIR SC 305 sensor, as

Fig. 4. Example of sensor image cropping to match FLIR SC305 field of view. Example of FLIR SC305 thermal image overlay on sensor visible image.

illustrated in Fig. 4.

Three repetitions were made for each measurement with the FLIR SC305. A manually segmented ROI mean temperature was obtained per repetition. The result of each measurement was defined as the average value of the repetitions.

2.2.2. Experimental setup

Two-year-old potted almond trees (*Prunus dulcis*) were used for the experimental setup. Trials were performed on four trees located in Cartagena, Murcia, Spain (37°36′00.4″N 0°58′46.3″W). Two drip irrigation emitters per tree (4 L/h) were installed for non-limiting water conditions. Two measurements a day were made with the sensor and the commercial thermal camera at two different time periods, one in the morning (9 GMT + 2) and the other at midday (14 GMT + 2), when the difference of temperature between the ambient and the crop canopy is significant. In the case of this article, the sensor was assembled on a stand support, but it could be adapted to use in land vehicles or as a handheld sensor. Concretely, both measuring equipment were placed on an articulated stainless steel stand support. It allowed the height and orientation of the cameras to be adjusted. The different elements of the experimental setup are identified in Fig. 5.

2.2.3. Thermal calibration

The calibration of the thermal sensor and the commercial thermal camera was performed by using a black body (Model 1000 Portable Calibration Source for Field Use, Everest Interscience Inc., 2888 English Road, Chino Hills, CA 91709, USA) ("1000 Calibration Source") with an accuracy of ±0.3 °C. Different temperature measurements of the black body were obtained with both sensors at a very short distance (5 cm), as specified by the manufacturer, while the temperature of the black body itself was recorded as the reference temperature. The temperature measured by the sensor corresponded to the mean of the central 10x10 pixel region of the temperature matrix, whereas that of the FLIR SC305 camera corresponded to the mean of the manual selected central region of the image.

3. Results and discussion

3.1. Sensor characterization

The characterization of the sensor is a critical process whose objective is to determine the temporal evolution of the temperature measurement between cycles of Flat Field Correction (FFC) of the thermal sensor. This internal calibration process is performed to adjust the measurement when the temperature of the sensor varies. A measurement process consisting of several series of repetitions corresponding to different FFC events of the sensor was carried out. In Fig. 6, the time evolution of the sensor temperature measurement is presented. The temperature oscillated remarkably around the FFC event, which was considered transient in the measurement process. The sensor presented a heating curve until its measurement was stabilized.

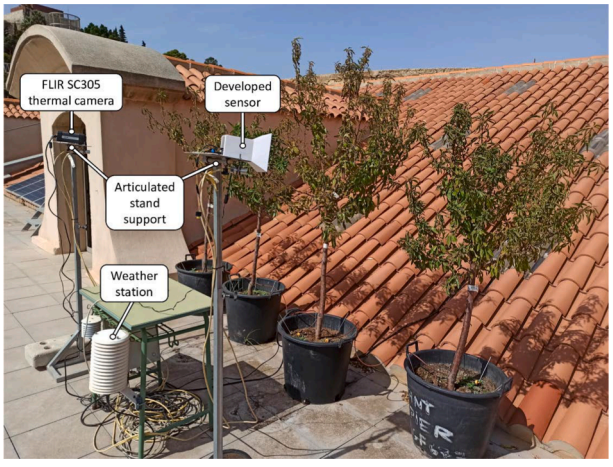

Fig. 5. Experimental setup.

Ten FFC cycles of 300 frames each were performed, with an average sensor refresh time of 0.54 s. At the moments following the FFC, there was a temperature variation of up to 1.5 °C, which triples the temperature range measured throughout each cycle, which was approximately 0.5 °C. Therefore, it was decided to define a transient time after the FFC event to filter the measurements in each series. This time was measured in multiple cycles of several tests and resulted to be approximately 30 s. In addition, some initial frames, corresponding to the heating process of the sensor, were not taken into account. To specify the number of frames to be ignored, a temperature stabilisation test consisting of three consecutive measurement processes in which a series of 500 frames were measured was carried out.

According to Fig. 7, it appears that, in the first measurement, the temperature did not stabilize, but in the following two measurements it did after the transient. Specifically, the temperature in these two latter cases was in the range of 24.25 °C to 24.75 °C. Hence, to avoid the lack of stabilization, when making the first measurement of a batch, it was decided to perform a complete measurement process as a warm-up which is not considered in the analysis. Additionally, the number of initial frames was chosen to be 150, corresponding to 81 s for the usual refreshing time of the sensor, in order to mitigate the effect that could occur between two consecutive measurements.

The experiments mentioned above were conducted indoors, so in search of external sources of error derived from environmental conditions, which could influence the measurement, the effect of the wind on the sensor was analysed. Indoor tests were undertaken to study the effect of wind in controlled and isolated conditions by using a fan as the wind source. The behaviour of the sensor was compared depending on the existence or not of the source of error by means of multiple tests of 10 FFC cycles, filtering the transient, and 300 frames per cycle.

In Fig. 8a and 8b, it can be seen that the action of the fan significantly affected the temperature measured by the sensor. With the fan off, the temperature of each cycle oscillated within a range of 0.5 °C and for all the cycles, without considering the first one due to not having carried out the previous warm-up process, in a range inferior to 1 °C. Instead, when the fan was turned on, the temperature range measured within each cycle was increased to 6 °C and the total range to 14 °C. The oscillating behaviour of the temperature measurement was due to the rotation cycle of the fan head. The thermal sensor has a very small size, which makes it ideal for a large number of applications. However, this is also a disadvantage, since such a low mass leads to small thermal inertia, which makes it particularly sensitive to thermal drift. As a way to correct the problem, a perimeter shield housing as shown in Fig. 9, was designed to minimize the wind effect on the thermal sensor without affecting the field of view of the sensor cameras. This solution was previously adopted in other research (Osroosh et al., 2018) in order to protect the sensor from raindrops.

New tests were made to assess the effectiveness of the improvement. In compliance with Fig. 8c and 8d, it was noted that with the housing the effect of the fan was significantly reduced. When the fan was oriented so that the airflow reached the sensor from the side, as it had been in the previous comparative tests, the range of temperature variation was similar to that obtained with the fan off, whereas placing the fan frontally the effect was also reduced, although not as effectively.

The resulting sensor measurement procedure is performed in a continuous and controlled mode. When the order is executed, the sensor automatically performs 3 series of 80 measurements associated with three different FFC calibration events, from which it filters the measurements corresponding to the transient, as seen in Fig. 10.

As a result, several measures were obtained from each series from which the statistical parameters of interest were obtained. Specifically,

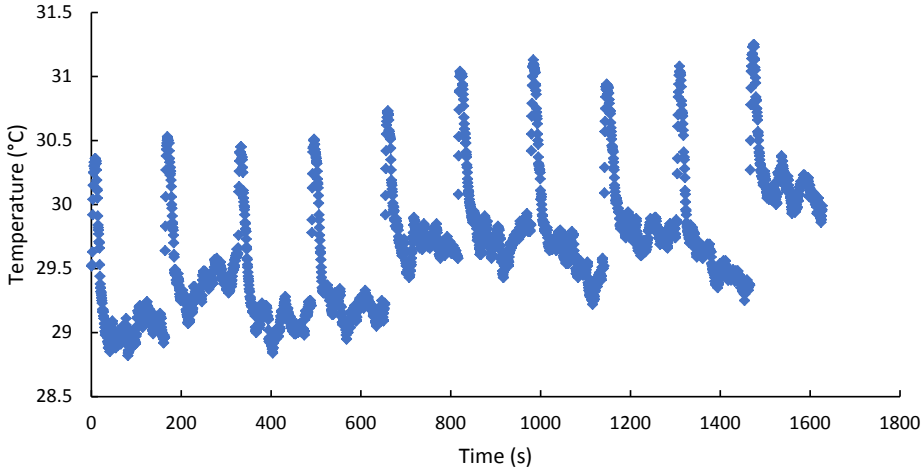

Fig. 6. Time evolution of the sensor temperature measurement.

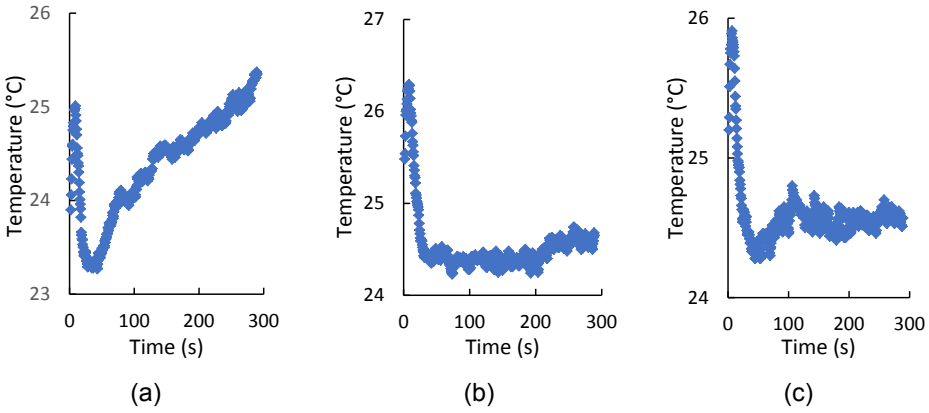

Fig. 7. Consecutive initial temperature stabilisation tests: (a) first, (b) second and (c) third.

for each measurement of each series, the mean of the seven median values of the masked temperature matrix was calculated. As a filter for the masked temperature matrix, to mitigate the effect of a possible error in the matching of images, extreme values were eliminated: those above the mean plus three times the standard deviation. For each series, the median, mean and standard deviation were calculated. As representative values of the measurement of each almond tree at a certain hour, the mean and standard deviation of the medians of the three series and the mean of the standard deviations of the series were calculated.

3.2. Evaluation of the sensor performance on the leaf temperature determination

In order to evaluate the performance of the sensor, the measurement procedure was undertaken in the almond trees. Before carrying out the leaf temperature measurements, a calibration process with the black body was executed. Calibration curves were obtained for both cameras with 20 points measured outdoors, as depicted in Fig. 11.

The average temperature difference between the sensor and the black body in the calibration measurements was 0.57 °C and the maximum difference was 1.5 °C. For the FLIR SC305, the average difference was 0.33 °C and the maximum was 0.62 °C.

Regarding the leaf temperature measurements, those obtained with the SVM segmentation model were not further analysed because of their similarity to the Deep Learning model. The mean difference of all measurements taken between them was 0.07 °C, the median 0.04 °C and the maximum 0.7 °C. In Fig. 12, an example of a measurement comparison between segmentation models is illustrated. The original visible and thermal images are shown, as well as the segmented images with the corresponding temperature value.

Beginning on the 271 DOY of 2020, nineteen measurements were made (ten in the morning and nine at midday) over ten days on the four almond trees, making a total of seventy-six comparable temperature measurements between the developed sensor and the reference thermal camera. These measurements are presented in Fig. 13.

The temperature obtained from the developed sensor and the commercial thermal camera showed an R-squared correlation of 0.63. In absolute terms, the temperature differences obtained in the test were, in all cases, within the accuracy range of the manufacturer of the low-cost thermal sensor (±5 °C). The maximum error found was 4.5 °C, the mean difference 1.2 °C and the median difference 0.9 °C. García-Tejero et al. (García-Tejero et al., 2018) compared a low-cost thermal camera (FLIR One) and a conventional thermal camera (FLIR SC660). The former integrates a thermal sensor (FLIR Lepton 2.5), which is similar to that of the thermal camera of our proposed design, but with lower resolution. They obtained a maximum difference between cameras of 4 °C, which is in agreement with the 4.5 °C reported here. Nonetheless, they found a better R-squared correlation of 0.9, that could be explained by a notably higher temperature range of the measurements, which was of 15 °C instead of 9.3 °C of our case.

At midday, when the difference of temperature between the ambient and the crop canopy is substantial, the time of maximum stomatal activity for most crops is found (Jackson et al., 1981). Thus, thermal measurements are typically made at midday (García-Tejero et al., 2018).

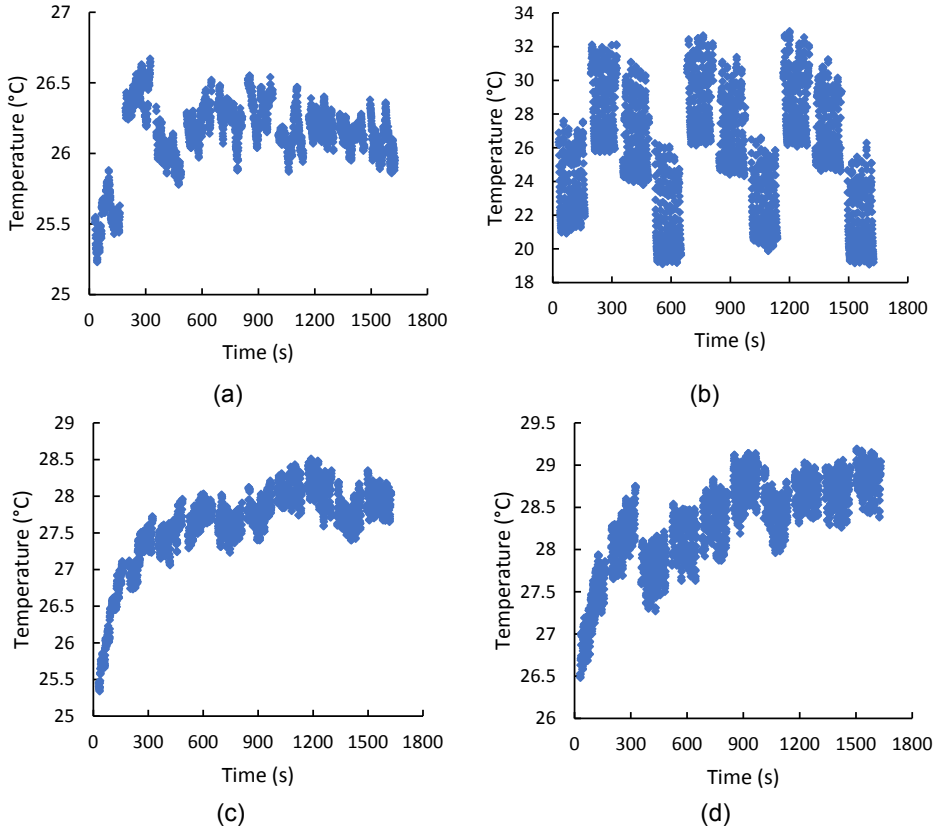

Fig. 8. Indoor wind effect test: (a) fan off; (b) fan on; (c) fan on from the side with protective housing; and (d) fan on from front with protective housing.

Fig. 9. Perimeter shield housing.

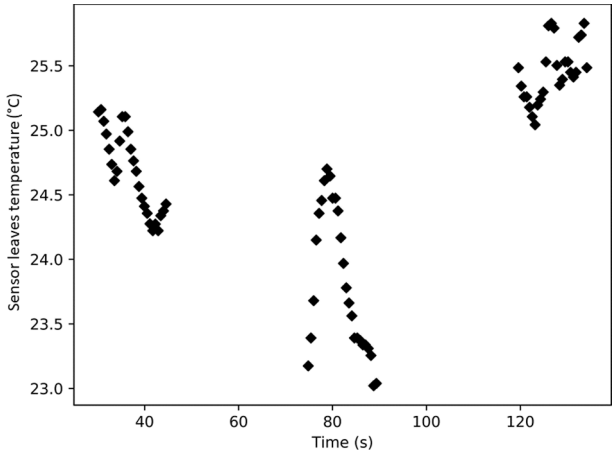

Fig. 10. Example of sensor measurement with the filtered transient.

The midday data were disaggregated to examine the behaviour of the sensor at that time and are presented in Fig. 14. Considering the results, it can be inferred that the midday measurements showed an acceptable R-squared correlation (0.75) between the developed sensor and the commercial reference thermal camera.

Furthermore, the standard deviation in all the measurements of the developed sensor were examined to investigate whether it is related to the temperature difference with the reference thermal camera. In Fig. 15, the standard deviation of the developed sensor, both between different series of the same measurement (15a) and between repetitions within the same series (15b), was compared with the temperature differences between sensors.

The standard deviation between measurements of the same series and between different series was significantly high, with respect to the temperature values measured, in certain cases. However, it is clear from Fig. 15 that this did not directly lead to a greater difference between the temperatures of the sensors compared. For this to be the case, the temperature difference would have increased with the standard deviation in the measurement. Due to the measurement procedure, it was possible to average the result and achieve a reduced error even with large standard deviations in the measurement series. For examples, on the one hand, a measurement is resorted to in which the temperature difference was 0.6 °C, while the standard deviation between series was 6.7 °C and the average of the standard deviations of the series was of 1.8 °C. On the other hand, the measure in which the greater difference of temperature between both sensors was obtained (4.5 °C), presented a standard deviation between the series of 0.5 °C and the average of the

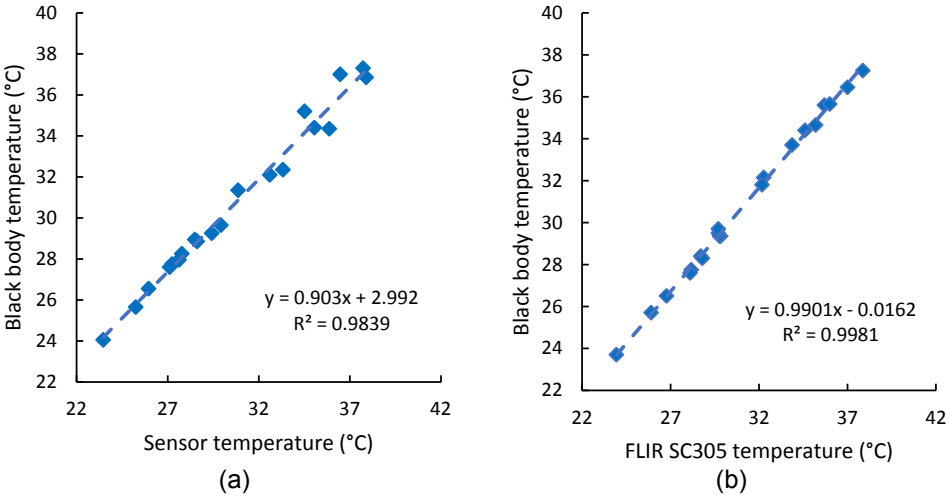

Fig. 11. New calibration curves with black body: (a) sensor and (b) FLIR SC305.

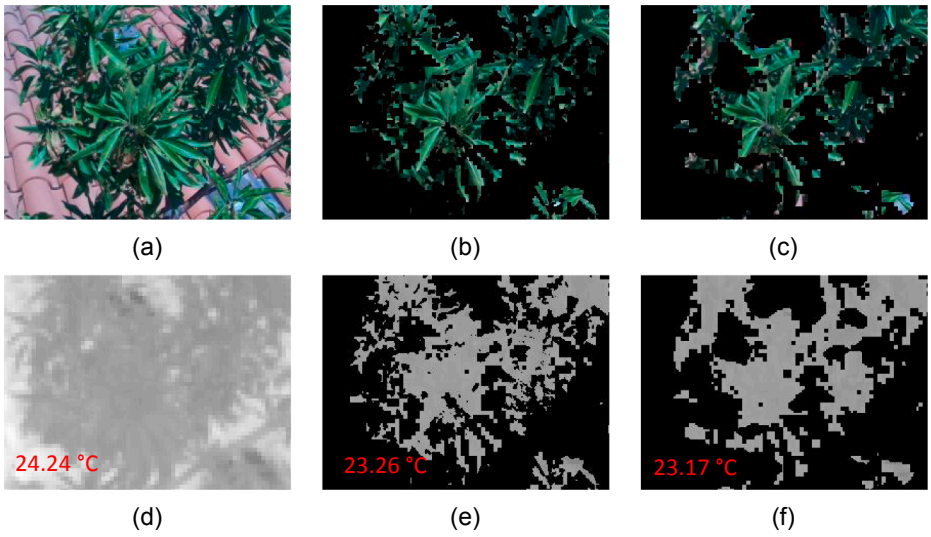

Fig. 12. Example of a measurement comparison between segmentation models: (a) visible image; (b) SVM model segmentation mask; (c) Deep Learning model segmentation mask; (d) thermal image with mean temperature; (e) thermal image masked with SVM model and ROI's mean temperature; and (f) thermal image masked with Deep Learning model and ROI's mean temperature.

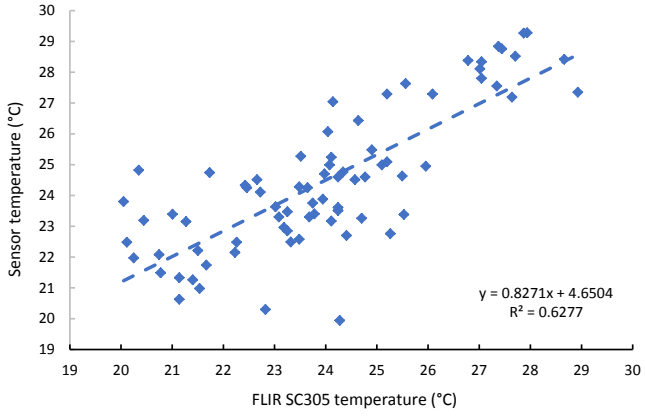

Fig. 13. Leaf temperatures measured with the developed sensor vs FLIR SC305.

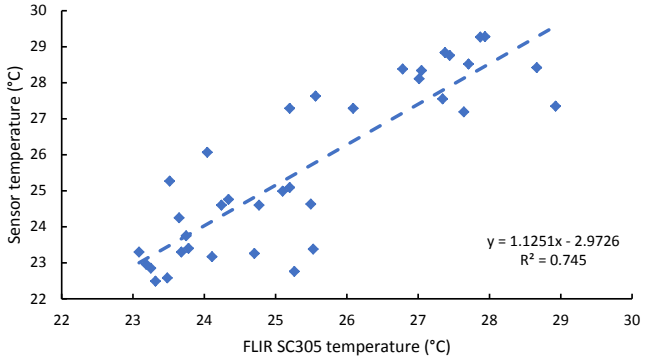

Fig. 14. Leaf temperatures measured at midday by the developed sensor vs FLIR SC305.

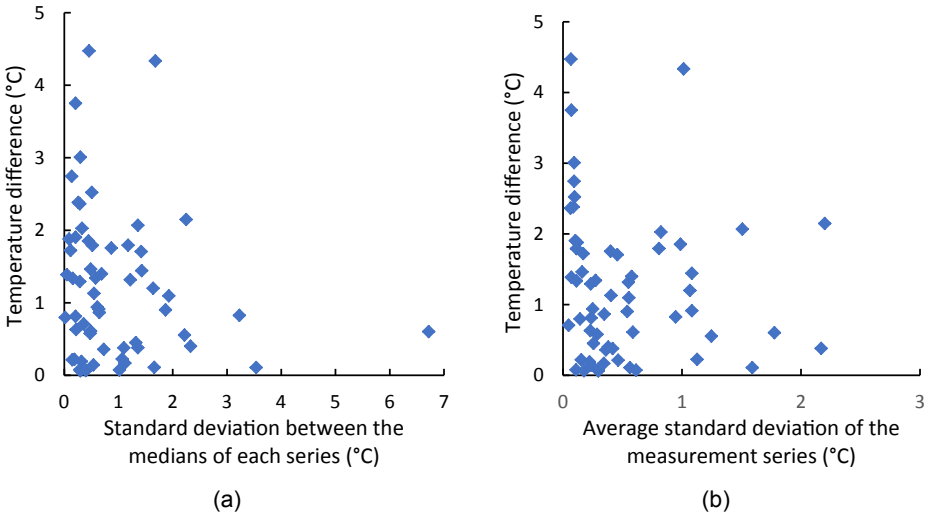

Fig. 15. (a) Temperature difference between sensors vs. standard deviation between the medians of each series of measurements and (b) temperature difference between sensors vs. average standard deviation of the measurement series.

standard deviations of the series of 0.1 °C. Therefore, it was not possible to establish a criteria that allowed filtering results according to great variability in the measurement of the sensor within the same series of measurements or between them. Simultaneously, this makes it possible to affirm that variability in measurements was not the cause of poor results. Hence, as wind is an external factor that introduces variability in the measurement, as demonstrated in indoor tests, it can be stated that it cannot be responsible for such errors. Consequently, there must be a factor that causes a difference in the measurement of both sensors without penalising the constancy of the measurement. This factor can be environmental and derived from the time between taking measurements with both sensors or due to the precision of the low-cost thermal sensor used.

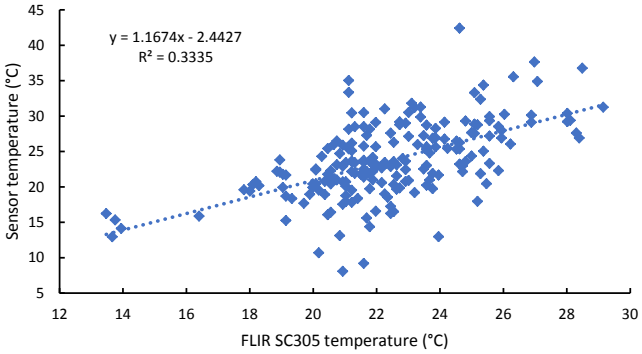

Fig. 16. Leaf temperatures measured by the sensor vs FLIR SC305.

3.3. Considerations on the measurement procedure

In addition to the errors obtained between the developed sensor and FLIR SC305, the measurement procedure had one disadvantage to be considered, which is the large volume of measurements required. This significantly affects the processing and measurement time and the volume of information to be saved and communicated. A new test was carried out with a lower number of measurements per series in order to ascertain the feasibility of reducing this drawback. The number of frames per cycle was reduced from 80 to 65, which, by filtering the transient, resulted in a reduction from 25 to 10 measurements per series. However, the results obtained on two days of measurement were inconsistent.

The sensor's measurement process was initially defined as an isolated one, which would have led to a scenario with a minimum need for measurements. The operator was in charge of ordering the capture by pressing the corresponding switch. In this way, three repetitions were taken per measurement, separated in time by a few seconds. The capture sequence was carried out once the warmup LED indicated that the system was ready to measure, but the time was not fixed exactly. This meant that there was no control over the timing of the sensor cycle in which the measurement was made. Moreover, wind protection housing was not implemented. The result of each measurement was defined as the average value of the repetitions. Before proceeding with the measurements, the calibration process was accomplished. The measures began on the 122 DOY of 2020 and lasted 25 days. The comparative leaf temperature results between the two sensors showed a low correlation, as illustrated in Fig. 16.

Hence, even though this protocol offered a smaller volume of information to be processed with the consequent time advantage, given the results, the behaviour of the sensor made it unfeasible. Some results were irrational and, in any case, worse than those presented previously, reaching a maximum difference of 17.8 °C, an average of 3.4 °C and a median of 2.4 °C.

4. Conclusions

Image-based sensors are promising tools for the determination of vegetative status indexes. The use of UAVs equipped with hyperspectral cameras for the management of large crops is now becoming widespread. However, these systems cannot be used to manage some irrigation strategies, such as those which need automated and continuous measurements. Besides, the use of commercial thermal cameras for monitoring installations with several measurement points can be decisively expensive in terms of equipment. Recently, some radiometric modules with reduced cost and limited resolution have become available. These modules can be used for leaf temperature monitoring control, which would reduce the limitations described above. To determine the suitability of these devices in the field of precision agriculture, this paper describes the design of an image-based leaf temperature sensor using a low-cost radiometric module. Artificial intelligence-based image segmentation models were implemented and the thermal module used (FLIR Lepton 3.5) has been characterised. The device presented allows an automatic measurement, avoiding the need of specialized personnel to operate the thermal camera and the specific software for ROI segmentation and processing. This can be a determining factor for the

applicability of these systems in remote crop water status measurement. In addition, in order to evaluate the performance of the proposed development, the results obtained in almond trees under real conditions were compared with those of a high-profile thermal camera (FLIR SC305). The R-squared correlation obtained for the automatic measurements taken at midday, which is the most representative daily range of canopy activity, was 0.75, indicating a high level of confidence in the measurement results with respect to the higher resolution thermal cameras. The dynamic characterisation of the measurement process in low-cost radiometric modules has been described in this paper as a necessary step to use these devices as indicators of vegetative activity in precision agriculture applications. However, the measurement procedure described requires of a high number of repetitions to minimize the lack of stability of the thermal module measurement, which implies a large processing time. Additionally, it was concluded that a physical barrier was necessary to stabilise the measurement against the presence of wind. Radiometric calibration of the sensor would be necessary under fluctuating ambient temperature conditions to correct the effect of the high sensitivity of the sensor to external influences. Thus, low-cost thermal cameras have limitations that need to be considered when making absolute temperature measurements under real field conditions. Although this paper has shown that low-resolution thermal modules can be used under certain limitations, technological developments in this field suggest that radiometric modules with better resolution and performance will be available shortly, which will reduce the shortcomings here discussed.

Funding

This research was funded by the Agencia Estatal de Investigación (AEI) under project numbers: AGL2016-77282-C3-3-R, and PID2019-106226-C22 AEI/https://doi.org//10.13039/501100011033. FPU17/05155, FPU19/00020 have been granted by Ministerio de Educación y Formación Profesional.

CRediT authorship contribution statement

Jaime Giménez-Gallego: Conceptualization, Data curation, Investigation, Methodology, Software, Visualization, Writing - original draft. **Juan D. González-Teruel:** Methodology, Validation, Writing - review & editing. **Fulgencio Soto-Valles:** Data curation, Resources, Supervision, Validation, Writing - review & editing. **Manuel Jiménez-Buendía:** Data curation, Resources, Software, Supervision, Validation, Writing - review & editing. **Honorio Navarro-Hellín:** Formal analysis, Methodology, Supervision, Validation, Writing - review & editing. **Roque Torres-Sánchez:** Conceptualization, Data curation, Formal analysis, Funding acquisition, Investigation, Methodology, Project administration, Resources, Validation, Writing - original draft.

Declaration of Competing Interest

The authors declare the following financial interests/personal relationships which may be considered as potential competing interests: Honorio Navarro-Hellín reports a relationship with Widhoc Smart Solutions that includes: employment.

Acknowledgments

The authors would like to acknowledge the support of Miriam Montoya Gómez in language assistance.

References

1000 Calibration Source [WWW Document], n.d. URL http://www.everestinterscience.com/products/0-CalibrationSource/MODEL0-SPECIFICATIONS.pdf (accessed 4.9.20).

Aasen, H., Honkavaara, E., Lucieer, A., Zarco-Tejada, P.J., 2018. Quantitative remote sensing at ultra-high resolution with UAV spectroscopy: A review of sensor technology, measurement procedures, and data correctionworkflows. Remote Sens. 10, 1–42. https://doi.org/10.3390/rs10071091.

Achanta, R., Shaji, A., Smith, K., Lucchi, A., Fua, P., Süsstrunk, S., 2012. SLIC superpixels compared to state-of-the-art superpixel methods. IEEE Trans. Pattern Anal. Mach. Intell. 34, 2274–2281. https://doi.org/10.1109/TPAMI.2012.120.

Azlah, M.A.F., Chua, L.S., Rahmad, F.R., Abdullah, F.I., Alwi, S.R.W., 2019. Review on techniques for plant leaf classification and recognition. Computers 8. https://doi.org/10.3390/computers8040077.

Azorín, P.R., García, J.G., 2020. The productive , economic, and social efficiency of vineyards using combined drought - tolerant rootstocks and efficient low water volume deficit irrigation techniques under mediterranean semiarid conditions 12. https://doi.org/10.3390/su12051930.

Bausch, W., Trout, T., Buchleiter, G., 2011. Evapotranspiration adjustments for deficit-irrigated corn using canopy temperature: A concept. Irrig. Drain. 60, 682–693. https://doi.org/10.1002/ird.601.

Berni, J.A.J., 2009. Determinación del Estado Hídrico de la Vegetación mediante Teledetección basada en Vehículos Aéreos No Tripulados. Universidad de Córdoba.

Berni, J.A.J., Zarco-Tejada, P.J., Suárez, L., Fereres, E., 2009. Thermal and narrowband multispectral remote sensing for vegetation monitoring from an unmanned aerial vehicle. IEEE Trans. Geosci. Remote Sens. 47, 722–738. https://doi.org/10.1109/TGRS.2008.2010457.

Bianco, S., Cadene, R., Celona, L., Napoletano, P., 2018. Benchmark analysis of representative deep neural network architectures. IEEE Access 6, 64270–64277. https://doi.org/10.1109/ACCESS.2018.2877890.

Blanco, V., Blaya-Ros, P.J., Castillo, C., Soto-Vallés, F., Torres-Sánchez, R., Domingo, R., 2020. Potential of UAS-based remote sensing for estimating tree water status and yield in sweet cherry trees. Remote Sens. 12 https://doi.org/10.3390/RS12152359.

Blaya-Ros, P.J., Blanco-Montoya, V., Torres-Sánchez, R., González-Teruel, J.D., Soto-Valles, F., Toledo-Moreo, A.B., Jiménez-Buendía, M., Domingo-Miguel, R., 2019. Sistema para la asistencia en la orientación de termo-radiómetros para procesos de medida de temperatura foliar. XXXVII Congr. Nac. Riegos, Don Benito. https://doi.org/10.17398/AERYD.2019.A18.

Blaya-Ros, P.J., Blanco, V., Domingo, R., Soto-Valles, F., Torres-Sánchez, R., 2020. Feasibility of low-cost thermal imaging for monitoring water stress in young and mature sweet cherry trees. Appl. Sci. 10 https://doi.org/10.3390/APP10165461.

Blonquist, J.M., Norman, J.M., Bugbee, B., 2009. Automated measurement of canopy stomatal conductance based on infrared temperature. Agric. For. Meteorol. 149, 1931–1945. https://doi.org/10.1016/J.AGRFORMET.2009.06.021.

Boykov, Y.Y., Jolly, M.-P., 2001. InteractiveGraph Cuts for Optimal Boundary & Region Segmentation of Objects in N-D Images. In: Proc. 8th IEEE Int. Conf. Comput. Vis. pp. 105–112.

Brigger, P., Hoeg, J., Unser, M., 2000. B-spline snakes: A flexible tool for parametric contour detection. IEEE Trans. Image Process. 9, 1484–1496. https://doi.org/10.1109/83.862624.

Camino, C., Zarco-Tejada, P.J., Gonzalez-Dugo, V., 2018. Effects of heterogeneity within tree crowns on airborne-quantified SIF and the CWSI as indicators of water stress in the context of precision agriculture. Remote Sens. 10, 1–18. https://doi.org/10.3390/rs10040604.

Cerutti, G., Kurtz, C., Vacavant, A., Tougne, L., Weber, J., Grand-Brochier, M., 2015. Tree Leaves Extraction in Natural Images: Comparative Study of Preprocessing Tools and Segmentation Methods. IEEE Trans. Image Process. 24, 1549–1560. https://doi.org/10.1109/tip.2015.2400214.

Cerutti, G., Tougne, L., Mille, J., Vacavant, A., Coquin, D., 2013. Understanding leaves in natural images - A model-based approach for tree species identification. Comput. Vis. Image Underst. 117, 1482–1501. https://doi.org/10.1016/j.cviu.2013.07.003.

Chan, T.F., Vese, L.A., 2001. Active contours without edges. IEEE Trans. Image Process. 10, 266–277. https://doi.org/10.1109/83.902291.

Chen, C., 2015. Determining the leaf emissivity of three crops by infrared thermometry. Sensors (Switzerland) 15, 11387–11401. https://doi.org/10.3390/s150511387.

Cheng, Y., 1995. Mean Shift, Mode Seeking, and Clustering. IEEE Trans. Pattern Anal. Mach. Intell. 17, 790–799. https://doi.org/10.1109/34.400568.

Comaniciu, D., Meer, P., Member, S., 2002. Mean shift: a robust approach toward feature space analysis. IEEE Trans. Pattern Anal. Mach. Intell. 24, 603–619.

Costa, J.M., Grant, O.M., Chaves, M.M., 2013. Thermography to explore plant-environment interactions. J. Exp. Bot. 64, 3937–3949. https://doi.org/10.1093/jxb/ert029.

Couprie, C., Grady, L., Najman, L., Talbot, H., 2009. Power watersheds: A new image segmentation framework extending graph cuts, random walker and optimal spanning forest. In: Proceedings of the IEEE International Conference on Computer Vision, pp. 731–738.

DeJonge, K.C., Taghvaeian, S., Trout, T.J., Comas, L.H., 2015. Comparison of canopy temperature-based water stress indices for maize. Agric. Water Manag. 156, 51–62. https://doi.org/10.1016/j.agwat.2015.03.023.

Dougherty, E., Beucher, S., Meyer, F., 2019. The Morphological Approach to Segmentation: The Watershed Transformation, in: Mathematical Morphology in Image Processing. CRC Press, pp. 433–481. https://doi.org/10.1201/9781482277234-12.

Felzenszwalb, P.F., Huttenlocher, D.P., 2004. Efficient graph-based image segmentation. Int. J. Comput. Vis. 59, 167–181. https://doi.org/10.1023/B:VISI.0000022288.19776.77.

Fereres, E., Soriano, M.A., 2006. Deficit irrigation for reducing agricultural water use. J. Exp. Bot. 58, 147–159. https://doi.org/10.1093/jxb/erl165.

Fernández García, I.F., Lecina, S., Ruiz-Sánchez, M.C., Vera, J., Conejero, W., Conesa, M. R., Domínguez, A., Pardo, J.J., Léllis, B.C., Montesinos, P., 2020. Trends and

Challenges in Irrigation Scheduling in the Semi-Arid Area of Spain. Water 12, 785. https://doi.org/10.3390/w12030785.
Fuentes, S., De Bei, R., Pech, J., Tyerman, S., 2012. Computational water stress indices obtained from thermal image analysis of grapevine canopies. Irrig. Sci. 30, 523–536. https://doi.org/10.1007/s00271-012-0375-8.
García-Tejero, I.F., Ortega-Arévalo, C.J., Iglesias-Contreras, M., Moreno, J.M., Souza, L., Tavira, S.C., Durán-Zuazo, V.H., 2018. Assessing the crop-water status in almond (Prunus dulcis mill.) trees via thermal imaging camera connected to smartphone. Sensors (Switzerland) 18, 1–13. https://doi.org/10.3390/s18041050.
Giménez-Gallego, J., González-Teruel, J.D., Jiménez-Buendía, M., Toledo-Moreo, A.B., Soto-Valles, F., Torres-Sánchez, R., 2019. Segmentation of multiple tree leaves pictures with natural backgrounds using deep learning for image-based agriculture applications. Appl. Sci. 10, 202. https://doi.org/10.3390/app10010202.
González-Teruel, J., Torres-Sánchez, R., Blaya-Ros, P., Toledo-Moreo, A., Jiménez-Buendía, M., Soto-Valles, F., González-Teruel, J.D., Torres-Sánchez, R., Blaya-Ros, P. J., Toledo-Moreo, A.B., Jiménez-Buendía, M., Soto-Valles, F., 2019. Design and Calibration of a Low-Cost SDI-12 Soil Moisture Sensor. Sensors 19, 491. https://doi.org/10.3390/s19030491.
Gutiérrez, S., Diago, M.P., Fernández-Novales, J., Tardaguila, J., 2018. Vineyard water status assessment using on-the-go thermal imaging and machine learning. PLoS One 13, 1–18. https://doi.org/10.1371/journal.pone.0192037.
Home - Keras Documentation [WWW Document], n.d. URL https://keras.io/ (accessed 4.9.20).
Howard, A.G., Zhu, M., Chen, B., Kalenichenko, D., Wang, W., Weyand, T., Andreetto, M., Adam, H., 2017. MobileNets: Efficient Convolutional Neural Networks for Mobile Vision Applications. Cornell Univ.
Idso, S.B., Jackson, R.D., Pinter, P.J., Reginato, R.J., Hatfield, J.L., 1981. Normalizing the stress-degree-day parameter for environmental variability. Agric. Meteorol. 24, 45–55. https://doi.org/10.1016/0002-1571(81)90032-7.
Jackson, R.D., Idso, S.B., Reginato, R.J., Pinter, P.J., 1981. Canopy Temperature as a Crop Water Stress Indicator. Water Resour. Res. 17, 1133–1138.
Jones, H.G., 2018. Thermal Imaging and Infrared Sensing in Plant Ecophysiology. In: Sánchez-Moreiras, A.M., Reigosa, M.J. (Eds.), Advances in Plant Ecophysiology Techniques. Springer, pp. 135–151. https://doi.org/10.1007/978-3-319-93233-0.
Kannan, N., Anandhi, A., 2020. Water Management for Sustainable Food Production. Water 12, 778. https://doi.org/10.3390/w12030778.
King, B.A., Shellie, K.C., 2016. Evaluation of neural network modeling to predict non-water-stressed leaf temperature in wine grape for calculation of crop water stress index. Agric. Water Manag. 167, 38–52. https://doi.org/10.1016/j.agwat.2015.12.009.
Krishna, G., Sahoo, R.N., Singh, P., Patra, H., Bajpai, V., Das, B., Kumar, S., Dhandapani, R., Vishwakarma, C., Pal, M., Chinnusamy, V., 2019. Application of thermal imaging and hyperspectral remote sensing for crop water deficit stress monitoring. Geocarto Int. https://doi.org/10.1080/10106049.2019.1618922.
Kullberg, E.G., DeJonge, K.C., Chávez, J.L., 2017. Evaluation of thermal remote sensing indices to estimate crop evapotranspiration coefficients. Agric. Water Manag. 179, 64–73. https://doi.org/10.1016/j.agwat.2016.07.007.
Li, H., Lee, W.S., Wang, K., 2016. Immature green citrus fruit detection and counting based on fast normalized cross correlation (FNCC) using natural outdoor colour images. Precis. Agric. 17, 678–697. https://doi.org/10.1007/s11119-016-9443-z.
Li, S.X., Chang, H.X., Zhu, C.F., 2010. Adaptive pyramid mean shift for global real-time visual tracking. Image Vis. Comput. 28, 424–437. https://doi.org/10.1016/j.imavis.2009.06.012.
Lin, G., Tang, Y., Zou, X., Cheng, J., Xiong, J., 2019a. Fruit detection in natural environment using partial shape matching and probabilistic Hough transform. Precis. Agric. 21, 160–177. https://doi.org/10.1007/s11119-019-09662-w.
Lin, G., Tang, Y., Zou, X., Xiong, J., Fang, Y., 2019b. Color-, depth-, and shape-based 3D fruit detection. Precis. Agric. 21, 1–17. https://doi.org/10.1007/s11119-019-09654-w.
López, A., Molina-Aiz, F.D., Valera, D.L., Peña, A., 2012. Determining the emissivity of the leaves of nine horticultural crops by means of infrared thermography. Sci. Hortic. (Amsterdam) 137, 49–58. https://doi.org/10.1016/j.scienta.2012.01.022.
Maes, W.H., Baert, A., Huete, A.R., Minchin, P.E.H., Snelgar, W.P., Steppe, K., 2016. A new wet reference target method for continuous infrared thermography of vegetations. Agric. For. Meteorol. 226–227, 119–131. https://doi.org/10.1016/j.agrformet.2016.05.021.
MATLAB official website [WWW Document], n.d. URL https://es.mathworks.com/products/matlab.html (accessed 6.18.19).
Naor, A., 2000. Midday stem water potential as a plant water stress indicator for irrigation scheduling in fruit trees. Acta Hortic. 447–454. https://doi.org/10.17660/ActaHortic.2000.537.52.
Noguera, M., Millán, B., Pérez-Paredes, J.J., Ponce, J.M., Aquino, A., Andújar, J.M., 2020. A new low-cost device based on thermal infrared sensors for olive tree canopy temperature measurement and water status monitoring. Remote Sens. 12 https://doi.org/10.3390/rs12040723.
Osroosh, Y., Khot, L.R., Peters, R.T., 2018. Economical thermal-RGB imaging system for monitoring agricultural crops. Comput. Electron. Agric. 147, 34–43. https://doi.org/10.1016/j.compag.2018.02.018.
Osroosh, Y., Peters, R.T., 2019. Detecting fruit surface wetness using a custom-built low-resolution thermal-RGB imager. Comput. Electron. Agric. 157, 509–517. https://doi.org/10.1016/j.compag.2019.01.023.
Otsu, N., 1979. A threshold selection method from gray-level histograms. IEEE Trans. Syst. Man. Cybern. SMC-9 62–66. https://doi.org/10.1109/tsmc.1979.4310076.
Poblete, T., Ortega-Farías, S., Ryu, D., 2018. Automatic coregistration algorithm to remove canopy shaded pixels in UAV-borne thermal images to improve the estimation of crop water stress index of a drip-irrigated cabernet sauvignon vineyard. Sensors (Switzerland) 18, 1–17. https://doi.org/10.3390/s18020397.
Python official website [WWW Document], n.d. URL https://www.python.org/ (accessed 12.11.19).
Rother, C., Kolmogorov, V., Blake, A., 2004. "GrabCut" - Interactive foreground extraction using iterated graph cuts, in: ACM Transactions on Graphics. ACM PUB27 New York, NY, USA , pp. 309–314. https://doi.org/10.1145/1015706.1015720.
Singh, V., Misra, A.K., 2017. Detection of plant leaf diseases using image segmentation and soft computing techniques. Inf. Process. Agric. 4, 41–49. https://doi.org/10.1016/j.inpa.2016.10.005.
Taghvaeian, S., Comas, L., DeJonge, K.C., Trout, T.J., 2014. Conventional and simplified canopy temperature indices predict water stress in sunflower. Agric. Water Manag. 144, 69–80. https://doi.org/10.1016/j.agwat.2014.06.003.
TensorFlow [WWW Document], n.d. URL https://www.tensorflow.org/ (accessed 4.9.20).
Torres-Sanchez, R., Navarro-Hellin, H., Guillamon-Frutos, A., San-Segundo, R., Ruiz-Abellón, M.C., Domingo-Miguel, R., 2020. A decision support system for irrigation management: Analysis and implementation of different learning techniques. Water (Switzerland) 12. https://doi.org/10.3390/w12020548.
Vicente-Guijalba, F., Martinez-Marin, T., Lopez-Sanchez, J.M., 2014. Crop phenology estimation using a multitemporal model and a kalman filtering strategy. IEEE Geosci. Remote Sens. Lett. 11, 1081–1085. https://doi.org/10.1109/LGRS.2013.2286214.
Ward, D., Moghadam, P., Hudson, N., 2019. Deep leaf segmentation using synthetic data. Br. Mach. Vis. Conf. 2018, BMVC 2018.
Weber, J., Lefèvre, S., Gançarski, P., 2011. Interactive Video Segmentation based on Quasi-Flat Zones. In: Proc. 7th Int. Symp. Image Signal Process. Anal. pp. 265–270.
Xia, C., Wang, L., Chung, B.-K., Lee, J.-M., 2015. In Situ 3D Segmentation of Individual Plant Leaves Using a RGB-D Camera for Agricultural Automation. Sensors 15, 20463–20479. https://doi.org/10.3390/s150820463.
Yang, W., Wang, X., Wheaton, A., Cooley, N., Moran, B., 2009. Automatic optical and IR image fusion for plant water stress analysis. In: 12th International Conference on Information Fusion. IEEE, Seattle, WA, USA, July 6-9, pp. 1053–1059.
Zhang, L., Zhang, Z., Luo, Y., Cao, J., Tao, F., 2020. Combining optical, fluorescence, thermal satellite, and environmental data to predict county-level maize yield in China using machine learning approaches. Remote Sens. 12 https://doi.org/10.3390/RS12010021.
Zhou, Z., Majeed, Y., Diverres Naranjo, G., Gambacorta, E.M.T., 2021. Assessment for crop water stress with infrared thermal imagery in precision agriculture: A review and future prospects for deep learning applications. Comput. Electron. Agric. https://doi.org/10.1016/j.compag.2021.106019.